


## Article

# Pressure-Dependent Structure of BaZrO<sub>3</sub> Crystals as Determined by Raman Spectroscopy

Dong-Hyeon Gim<sup>1</sup>, Yeahan Sur<sup>1</sup>, Yoon Han Lee<sup>1</sup>, Jeong Hyuk Lee<sup>1</sup>, Soonjae Moon<sup>2</sup>, Yoon Seok Oh<sup>3,\*</sup> and Kee Hoon Kim<sup>1,4,\*</sup> 

<sup>1</sup> Center for Novel States of Complex Materials Research, Department of Physics and Astronomy, Seoul National University, Seoul 08826, Korea; loyard@snu.ac.kr (D.-H.G.); yhsur2011@gmail.com (Y.S.); lyh9042@gmail.com (Y.H.L.); jeonghyuklee1508@gmail.com (J.H.L.)

<sup>2</sup> Department of Physics, Hanyang University, Seoul 04763, Korea; soonjmoon@hanyang.ac.kr

<sup>3</sup> Department of Physics, Ulsan National Institute of Science and Technology, Ulsan 44919, Korea

<sup>4</sup> Department of Physics and Astronomy, Institute of Applied Physics, Seoul National University, Seoul 08826, Korea

\* Correspondence: ysoh@unist.ac.kr (Y.S.O.); khkim@phya.snu.ac.kr (K.H.K.)

**Abstract:** The structure of dielectric perovskite BaZrO<sub>3</sub>, long known to be cubic at room temperature without any structural phase transition with variation in temperature, has been recently disputed to have different ground state structures with lower symmetries involving octahedra rotation. Pressure-dependent Raman scattering measurements can identify the hierarchy of energetically-adjacent polymorphs, helping in turn to understand its ground state structure at atmospheric pressure. Here, the Raman scattering spectra of high-quality BaZrO<sub>3</sub> single crystals grown by the optical floating zone method are investigated in a pressure range from 1 atm to 42 GPa. First, based on the analyses of the infrared and Raman spectra measured at atmospheric pressure, it was found that all the observed vibrational modes could be assigned according to the cubic  $Pm\bar{3}m$  structure. In addition, by applying pressure, two structural phase transitions were found at 8.4 and 19.2 GPa, one from the cubic to the rhombohedral  $R\bar{3}c$  phase and the other from the rhombohedral to the tetragonal  $I4/mcm$  phase. Based on the two pressure-induced structural phase transitions, the true ground state structure of BaZrO<sub>3</sub> at room temperature and ambient pressure was corroborated to be cubic while the rhombohedral phase was the closest second.

**Keywords:** barium zirconate; crystal structure; hydrostatic pressure; phase transition; Raman spectroscopy; infrared spectroscopy



**Citation:** Gim, D.-H.; Sur, Y.; Lee, Y.H.; Lee, J.H.; Moon, S.; Oh, Y.S.; Kim, K.H. Pressure-Dependent Structure of BaZrO<sub>3</sub> Crystals as Determined by Raman Spectroscopy. *Materials* **2022**, *15*, 4286. <https://doi.org/10.3390/ma15124286>

Academic Editor: Elhouichet Habib

Received: 21 May 2022

Accepted: 15 June 2022

Published: 17 June 2022

**Publisher's Note:** MDPI stays neutral with regard to jurisdictional claims in published maps and institutional affiliations.



**Copyright:** © 2022 by the authors. Licensee MDPI, Basel, Switzerland. This article is an open access article distributed under the terms and conditions of the Creative Commons Attribution (CC BY) license (<https://creativecommons.org/licenses/by/4.0/>).

## 1. Introduction

The dielectric oxide BaZrO<sub>3</sub> (BZO) with a perovskite structure exhibits a high structural stability, low thermal conductivity, and good refractory character such that it has been widely used, e.g., as a thermal barrier coating in aerospace industries [1] and as an inert crucible [2] and substrate [3] in laboratories. With an intrinsic dielectric constant as high as 43 [4], BZO shows enhanced piezoelectric properties upon being alloyed with BaTiO<sub>3</sub> [5]; Ba(Zr,Ti)O<sub>3</sub> has thus been widely used in lead-free piezoelectric actuators, transducers, and sensors and for wireless communications [6]. The application of BZO extends to the development of proton conductors [7], hydrogen separation reactors [8,9], and humidity sensors [10]. Befitting such a variety of applications requiring thermal and structural stability, BZO is known to maintain its cubic structure from 2 to 1473 K according to neutron and X-ray diffraction (XRD) studies [11,12].

However, several density functional theory (DFT) calculations have proposed that the true structural ground state may be of tetragonal  $I4/mcm$  symmetry due to the unstable antiphase antiferrodistortive (AFD) phonons of oxygen octahedra [13–15], and that the local tetragonal distortions can be averaged out and may have been undetectable in

the diffraction experiments which identified the cubic  $Pm\bar{3}m$  BZO structure. Seemingly supporting the DFT calculation results, a group of peaks was observed in the Raman spectra of BZO [16–19], although an ideal cubic perovskite has no first-order Raman-active optical phonons [20]. Hence, the observed Raman modes were interpreted to represent the short-ranged structural distortions in BZO [17–19]. Besides, in addition to the octahedral rotations, a Brillouin light-scattering experiment reported a loss of centro-symmetry due to local distortion in a commercially available BZO crystal in a temperature range from 93 to 1273 K [21]. Concrete interpretation of the vibrational modes observed in one of the highest-quality BZO single crystals is therefore necessary to resolve whether symmetry breaking is intrinsic or not.

There was another viewpoint which ascribed the observed Raman shifts to classical two-phonon modes from the cubic structure [16], as similarly demonstrated in other cubic perovskites such as  $\text{SrTiO}_3$  and  $\text{KTaO}_3$  [22,23]. Vibrational spectra measured by Raman scattering [16] and the phonon density of states from inelastic neutron scattering studies [24] indeed exhibited no sign of structural phase transitions in BZO in a wide temperature range (4–1200 K), suggesting that the cubic structure remains persistently. The absence of experimental evidence of any structural phase transition in BZO was attributed to zero-point fluctuations [11] and nonlocal exchange-correlation effects [25]. As an alternative scenario, it was also suggested that the energetic proximity of  $I4/mcm$ ,  $Imma$ , and  $R\bar{3}c$  structures each involving AFD distortions [25,26] can quench the manifestation of a certain distorted structure in BZO [27]. As the small energy differences among these tilt polymorphs can be effectively discriminated by means of external perturbation [26], the application of high pressure might be an effective way to sort out the energetic hierarchy of the competing polymorphs.

A previous study of pressure-dependent Raman scattering with BZO ceramics grown by the solid-state reaction method found two structural phase transitions at 9 and 23 GPa [19], which were assigned as a transition from a cubic to a rhombohedral  $R\bar{3}c$  phase and one from a rhombohedral to an orthorhombic  $Imma$  structure, respectively. On the other hand, another structural study on a commercial BZO powder with a synchrotron XRD measurement identified only one pressure-induced transition at 17.2 GPa from a cubic to a tetragonal  $I4/mcm$  phase [28]. As BZO ceramics grown by solid-state reaction can often possess local symmetry breaking by octahedra rotation due to the local strain at grain boundaries [6,29,30], the discrepancies in the number of phase transitions and the transition pressures reported by the two former high-pressure studies might originate from the polycrystalline nature of the samples. Therefore, a high-pressure experiment on a single crystal of BZO is desirable to resolve the discrepancy in the high-pressure results of the polycrystalline BZO specimens.

In this article, the Raman spectra of a BZO single crystal grown by the optical floating-zone method are investigated. Based on the comparison with infrared (IR) spectra and the DFT prediction on the phonon spectra, it is shown that all the Raman shifts of the BZO crystals can be successfully assigned to the two-phonon modes in the cubic phase. At higher pressures, there exist emergent first-order Raman modes, of which frequencies can be successfully assigned by the new crystal symmetry stabilized above 8.4 or 19.2 GPa. Based on the full assignment of the measured Raman spectra, it is concluded that  $\text{BaZrO}_3$  crystals undergo phase transitions from the cubic to the rhombohedral  $R\bar{3}c$  phase at 8.4 GPa, and subsequently to the tetragonal  $I4/mcm$  phase at 19.2 GPa.

## 2. Experimental Methods

### 2.1. Sample Preparation

High-quality  $\text{BaZrO}_3$  single crystals were grown by the optical floating-zone technique [31] in an  $\text{O}_2/\text{Ar}$  mixed gas environment. Polycrystalline  $\text{BaZrO}_3$  feed rods were prepared as stoichiometric  $\text{BaO}$  and  $\text{ZrO}_2$ , mixed, ground, pelletized, and sintered at 1650 °C for 24 h in air. The as-grown single crystals were annealed at 1650 °C in  $\text{O}_2$  flow. Each single crystal was cut into a circular disk with a typical diameter of 4 mm and thick-

ness of 1 mm. Figure 1 shows the XRD results of the polished (001) surface of the BaZrO<sub>3</sub> single crystal.

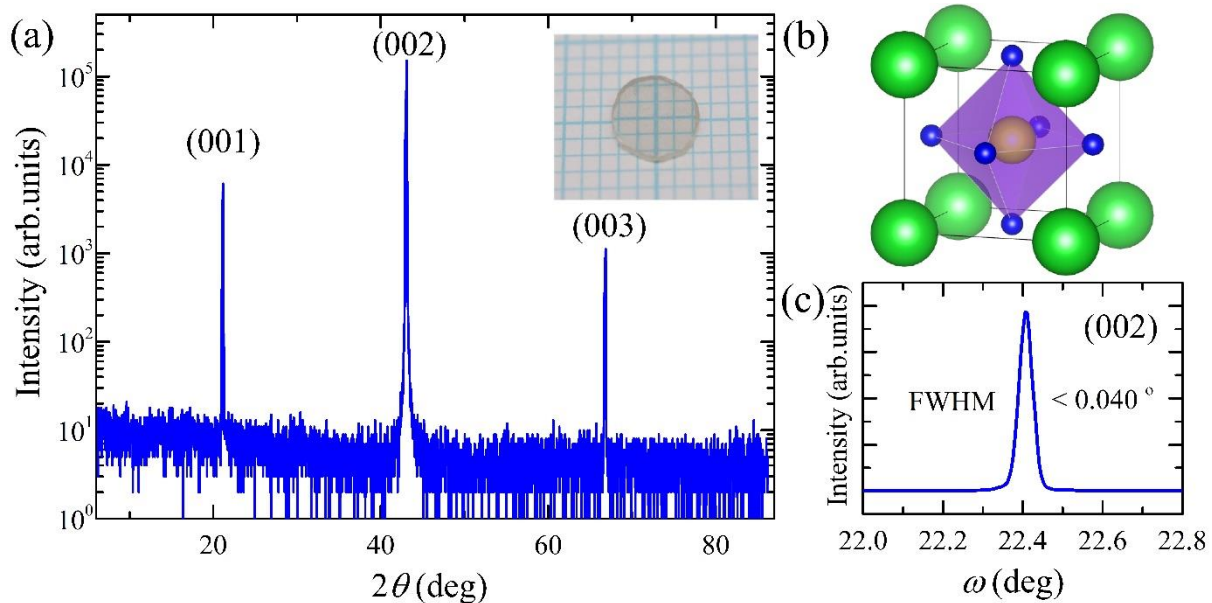


**Figure 1.** (a) The  $\theta$ - $2\theta$  scan of X-ray diffraction, showing (00 $l$ ) ( $l = 1, 2,$  and  $3$ ) peaks of the BaZrO<sub>3</sub> single crystal. The inset image shows the polished (001) surface of a BaZrO<sub>3</sub> single crystal on graph paper with a line spacing of 1 mm. (b) The cubic perovskite structure of BaZrO<sub>3</sub>, in which Ba (green spheres), Zr (yellow sphere), and oxygen ions (blue spheres) are coordinated. (c) The rocking curve ( $\omega$ -scan) measured at the (002) peak of the BaZrO<sub>3</sub> single crystal, exhibiting a full-width-half-maximum (FWHM) of less than  $0.040^\circ$ .

## 2.2. Pressure-Dependent Raman Spectroscopy Experiment

Back-scattered Raman spectra of the BZO single crystal were measured with a commercial Raman spectrometer (Nanobase, XperRam200<sup>TM</sup>) equipped with a  $20\times$  objective lens and a Nd:YAG laser with a 532 nm wavelength. To load the specimen into the diamond anvil cell (DAC) for the high-pressure Raman scattering experiments, the rectangular-shaped crystal was further cut into a small piece with a typical lateral size  $\sim 50\ \mu\text{m}$  and thickness  $\sim 5\ \mu\text{m}$ , the widest surface of which corresponds to the (001) plane. The pressure media comprised a liquid blend of methanol–ethanol with a 4:1 ratio. The applied pressure was estimated from an R1 photoluminescent line of ruby particles inserted inside a gasket next to the sample [32]. All the measurements were performed at room temperature (298 K), and a linearly polarized laser with the power of 0.6 mW was focused as a few  $\mu\text{m}^2$  beam spot on the diamond anvils. A polarizing filter was used to collect the parallel-polarized Raman spectra from the DAC, which are denoted by  $z(xx)\bar{z}$  in the figures. Here,  $x$  and  $z$  in the Porto's notation are parallel to the  $[100]_{\text{pc}}$  and  $[001]_{\text{pc}}$  axes of the pseudo-cubic (pc) lattice, respectively. The polarization of the incident laser light and outgoing scattering light, denoted by  $(xx)$  in this case, was maintained during the high-pressure measurements. Then, the DAC was decompressed to 1 GPa and compressed subsequently to collect the unpolarized Raman spectra without using the polarizing filter, which are denoted by  $z(xx + xy)\bar{z}$  in the figures. The parallel- and cross-polarized spectra at atmospheric pressure (Figure 2a,b) were measured outside the DAC using the polarizer filter. As a reference, the Raman spectra were also measured at atmospheric pressure in a BaZrO<sub>3</sub> polycrystalline pellet synthesized by the solid-state reaction method.

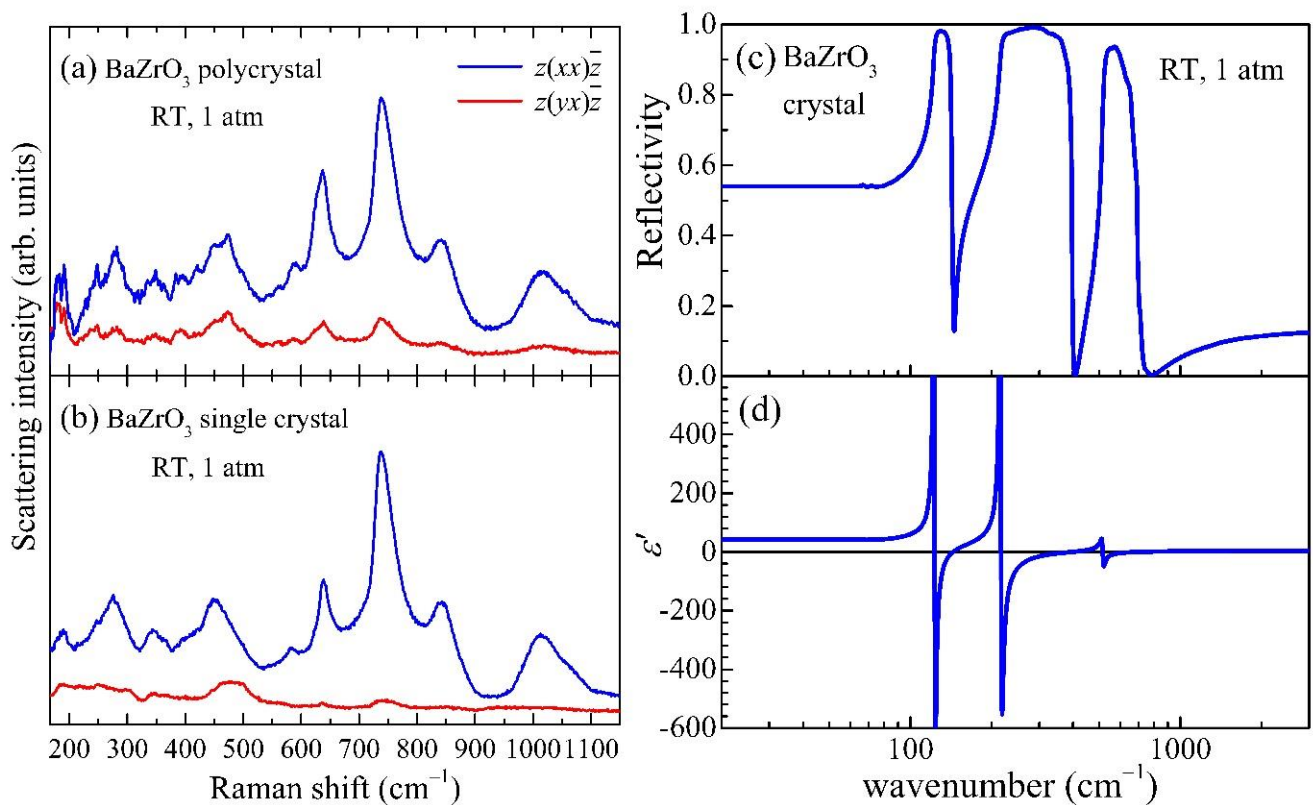


**Figure 2.** Vibrational spectra of BaZrO<sub>3</sub> measured at 1 atm. (a) Raman spectra of the BaZrO<sub>3</sub> polycrystal. (b) Raman spectra of the BaZrO<sub>3</sub> single crystal. (c) Infrared reflectivity spectrum of the BaZrO<sub>3</sub> single crystal. (d) Real part of the dielectric function  $\epsilon'$  of the BaZrO<sub>3</sub> single crystal obtained from the Kramers–Kronig transformation of the reflectivity data in (c).

### 2.3. Infrared Spectroscopy Experiment at the Atmospheric Pressure

In order to identify the exact energies of the zone-center optical phonons at atmospheric pressure, the IR reflectivity of the (001) plane of the BZO crystal was measured from 100 to 8000 cm<sup>-1</sup> using a Fourier-transform infrared spectrometer with in-situ gold overcoating technique. The real and imaginary parts of the dielectric function were obtained by Kramers–Kronig transformation of the reflectivity data. For the transformation, the complex dielectric function in the energy between 6000 and 50,000 cm<sup>-1</sup> obtained via spectroscopic ellipsometer was used. The reflectivity below the low-frequency cutoff of our measurements was extrapolated as a constant.

## 3. Results and Discussions

### 3.1. Vibrational Modes at Ambient Pressure

Figure 2a,b shows the polarized Raman spectra of a polycrystalline BaZrO<sub>3</sub> ceramic specimen and a BaZrO<sub>3</sub> single crystal, respectively. The overall features of the Raman spectra of the polycrystal qualitatively agree with those of the single crystal. Moreover, the Raman data in Figure 2b nearly reproduce the recently reported Raman scattering results on the single crystals at ambient pressure [16,31]. However, it should be noted that several additional peaks, located at 179, 248, 392, and 473 cm<sup>-1</sup>, are found only in the ceramic sample (Figure 2a) and are not clearly identified in the single crystal (Figure 2b). In the frequency window of those additional peaks, the single crystal data merely exhibit a hump or a broadened peak feature. This indicates that the additional peaks are broadened or suppressed in the single crystal. It is further noted that a larger number of peaks have been found in the previously reported Raman spectra of BZO ceramics [33,34]. The previous and current Raman spectra on the ceramic specimens thus indicate that the

scattering amplitudes of several additional phonons might be enhanced in the polycrystal, presumably due to the presence of local distortion or disorder.

It is well known that cubic perovskite with the space group  $Pm\bar{3}m$  allows three pairs of IR-active transverse optical (TO) and longitudinal optical (LO) phonon modes with the irreducible representation (irrep)  $\Gamma_4^-$ , and one degenerate IR- and Raman- inactive mode, called a silent mode, with irrep  $\Gamma_5^-$ . Because the three IR-active TO and LO phonons are only IR-active, the phonon frequencies as determined from the IR measurements can be useful for identifying phonons observed in the Raman spectra. Although two former measurements on the IR phonon spectra of BZO ceramics have been reported [34,35], their phonon frequencies exhibit sizable discrepancies up to  $110\text{ cm}^{-1}$ . Therefore, we have measured the IR reflectivity of the BZO single crystal and obtained the dielectric function after the Kramers–Kronig transformation as shown in Figure 2c,d. To identify the TO and LO frequencies, we have chosen peak and zero positions of the imaginary and real parts of dielectric functions, respectively. The frequencies of each TO and LO phonon obtained in this way are summarized in Table 1, which shows a good agreement with the latest first-principles calculations results [24,25]. Table 1 also summarizes the Raman peaks found in both ceramic (Figure 2a) and single-crystal (Figure 2b) specimens.

As evident from direct comparison with the IR data, the main Raman peak positions do not coincide with those zone-center  $\Gamma_4^-$  phonon frequencies, i.e.,  $\text{TO}_i$  and  $\text{LO}_i$  ( $i = 1-3$ ) mode frequencies, observed in the IR spectra. The fact that each  $\Gamma_4^-$  phonon remains Raman-inactive rules out the 45 crystal structures involving polar  $\Gamma_4^-$  displacements among the descendent 60 structures of the parental  $Pm\bar{3}m$  lattice [36]. In addition, we confirmed that the respective zone-boundary phonons at the  $R$ ,  $M$ , or  $X$  points with each energy predicted by the DFT computations [25] even fail to match with the measured Raman signals (as tabulated in Table 1). If the symmetry was lowered by distortion, at least one of the phonons located at the relevant  $k$ -points of cubic perovskites ought to become a Raman-active mode by relocating itself into the new  $\Gamma$  point in a folded zone of the supercell. For example, AFD  $R_4^+$  distortions can construct one of three symmetries, tetragonal  $I4/mcm$ , orthorhombic  $Imma$ , or rhombohedral  $R\bar{3}c$  structures, all of which can make  $R$  point phonons become Raman-active while leaving the original  $\Gamma$  point phonons Raman-inactive. However, it was found that the major peak frequencies in the measured Raman data disagree with those predicted by  $R$  or  $M$  point phonons (Table 1), clearly precluding the possibility of the other 15 lattice structures induced by AFD octahedra rotations with irreps  $M_3^+$  and  $R_4^+$  [37].

To fully understand the Raman spectra of the BZO crystal, the multi-phonon excitations must then be considered. In a Raman scattering process, the crystal with inversion symmetry indeed allows the creation of phonon pairs throughout the Brillouin zone (BZ) with opposite wave vectors, thus satisfying momentum conservation [38]. It is customary to regard combinations and overtones of phonons at the  $k$ -points with high symmetries such as  $\Gamma$ ,  $R$ ,  $M$ , and  $X$  of cubic perovskites since the scattering rates of two-phonon modes are weighted by the phonon density of states. It was indeed found that the two-phonon energies at  $\Gamma$ ,  $R$ , and  $M$  points are sufficient to assign the observed modes completely as summarized in Table 1; one can corroborate that  $\Gamma_4^-$  phonon frequencies as determined by IR spectroscopy comprise the majority of the assignments such as  $2\text{LO}_1$ ,  $2\text{TO}_2$ ,  $\text{TO}_1 + \text{TO}_2$ ,  $\text{TO}_2 + \text{TO}_3$ , and so on. On the other hand, solo phonons located at the zone center and boundaries, implying short-ranged or local lattice distortions [39,40], are unnecessary to explain the overall frequencies in the spectra. Therefore, the Raman scattering data at atmospheric pressure can be unambiguously identified by the multi-phonon excitations, consequently supporting a cubic  $Pm\bar{3}m$  symmetry as the structural ground state of the BZO crystal.

**Table 1.** A summary of the BaZrO<sub>3</sub> optical phonons at 1 atm. The first and second columns denote the observed Raman shifts, the third column lists the frequencies of the zone-center phonons determined from the IR spectra, and the fourth column shows the calculated frequencies of the relevant zone-boundary phonons in the literature. Frequencies are presented in wavenumbers (cm<sup>-1</sup>). Abbreviations in the fifth column are as follows: out-of-phase antiferrodistortive mode (OOP-AFD), A-type antiferroelectric mode (A-AFE), in-phase antiferrodistortive mode (IP-OOP), G-type antiferroelectric mode (G-AFE), scissor mode (Scissor), and Jahn–Teller-like rotation mode (JT-Rot).

Polycrystal Raman Shift	Single Crystal Raman Shift	Single Crystal IR Mode	Zone-Boundary Phonon (DFT)	Assignment
(Figure 2a)	(Figure 2b)	(Figure 2d)	[24,25]	
179	-			2X <sub>5</sub> <sup>+</sup> (Ba)
199	189			2M <sub>3</sub> <sup>+</sup> (O <sub>6</sub> )
248	-			2TO <sub>1</sub>
280	276			2LO <sub>1</sub>
348	343			TO <sub>1</sub> +TO <sub>2</sub>
392	-			LO <sub>2</sub>
444	447			2TO <sub>2</sub>
473	-			R <sub>5</sub> <sup>+</sup> +R <sub>5</sub> <sup>+</sup> (Ba <sub>2</sub> O <sub>6</sub> )
588	584			R <sub>4</sub> <sup>+</sup> +R <sub>3</sub> <sup>+</sup> (O <sub>6</sub> )
637	639			TO <sub>1</sub> + TO <sub>3</sub>
738	738			TO <sub>2</sub> + TO <sub>3</sub>
842	843			LO <sub>1</sub> + LO <sub>3</sub>
1017	1013			2TO <sub>3</sub>
		123		TO <sub>1</sub> (Ba–O)
		144		LO <sub>1</sub> (Ba–O)
		217		TO <sub>2</sub> (Zr–O)
		398		LO <sub>2</sub> (Zr–O)
		516		TO <sub>3</sub> (O–O)
		701		LO <sub>3</sub> (O–O)
			48	R <sub>4</sub> <sup>+</sup> (O <sub>6</sub> , OOP-AFD)
			87	X <sub>5</sub> <sup>+</sup> (Ba, A-AFE)
			95	M <sub>3</sub> <sup>+</sup> (O <sub>6</sub> , IP-AFD)
			106	R <sub>5</sub> <sup>+</sup> (Ba, G-AFE)
			373	R <sub>5</sub> <sup>+</sup> (O <sub>6</sub> , Scissor)
			545	R <sub>3</sub> <sup>+</sup> (JT-Rot.)

### 3.2. Raman Scattering at Higher Pressures

The Raman spectra of the BaZrO<sub>3</sub> single crystals measured at high pressures are displayed in Figure 3. It turns out that the overall Raman modes featured in the high-pressure spectra are analogous to those in [19], in which the Raman modes of BaZrO<sub>3</sub> ceramics were reported at high pressures. It is important to notice in Figure 3 that several new peaks start to appear from 8.4 GPa, and one of them at ~390 cm<sup>-1</sup> splits into two above 19.2 GPa (Figure 3c). All these findings indicate that there exist two major structural changes at ~8.4 and ~19.2 GPa. The mode frequencies as determined from Lorentzian fits are summarized in Figure 3 at each pressure. The symbols used in the legend indices in Figure 4a represent the Raman frequencies obtained from the Lorentzian fits in the phonon spectra shown in Figure 3a,b; note that the same symbols are used to represent the corresponding phonon modes in Figure 3a,b. It is found that all the newly-observed peaks above ~8.4 GPa can be assigned as the phonons stemming from the R point of the original cubic BZ (vide infra).

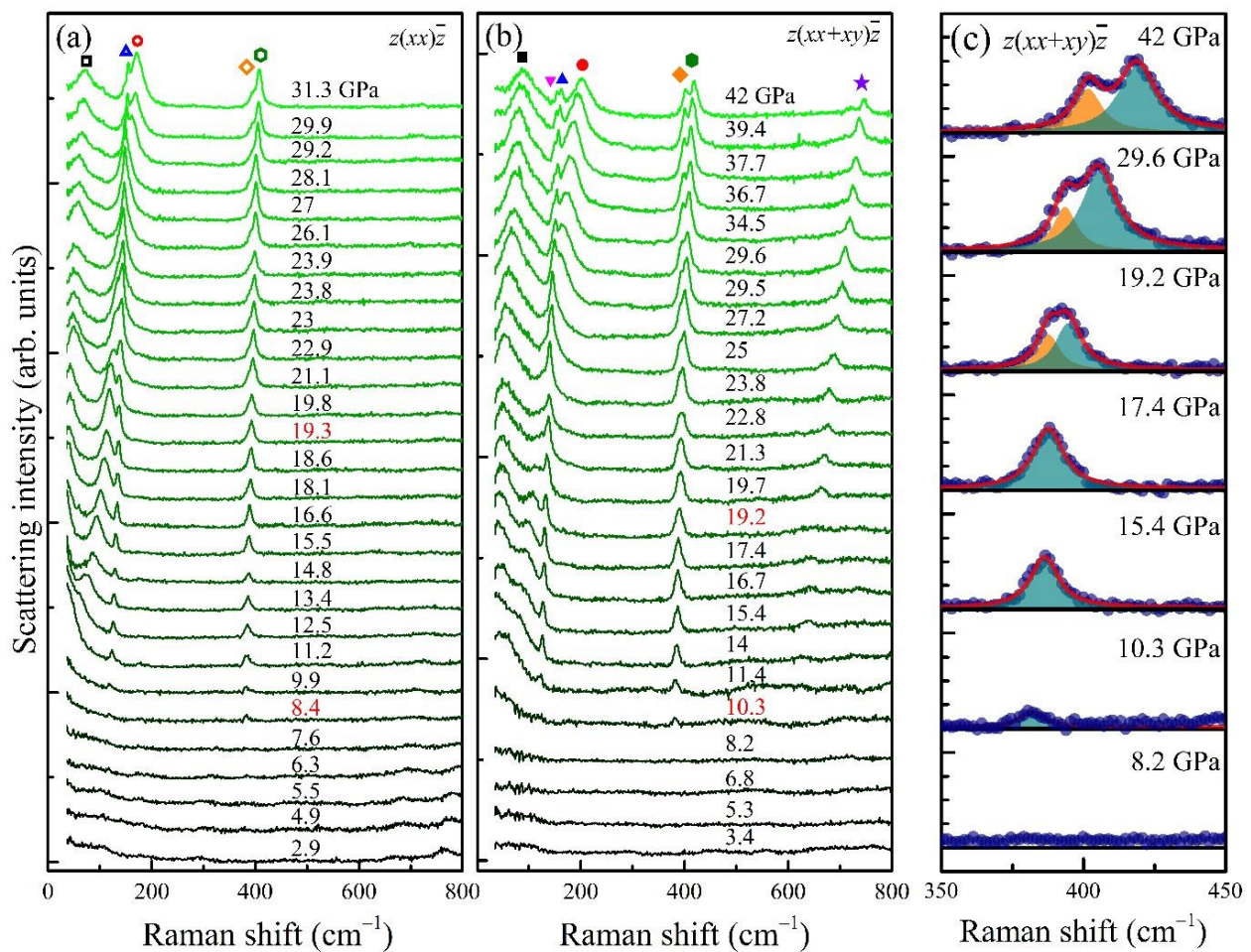


**Figure 3.** Pressure-dependent Raman scattering of the BaZrO<sub>3</sub> single crystal: (a)  $z(xx)\bar{z}$  spectra measured with the polarizing filter; (b)  $z(xx+xy)\bar{z}$  spectra measured without the polarizing filter. The Raman phonon modes are indicated as the symbols in (a,b), of which frequencies obtained from the fitting process are summarized in Figure 4a with the same type of symbols. The pressures at which a structural phase transition occurs are colored in red. (c) The evolution of the phonon mode, stemming from an  $R_5^+$  scissor mode (Raman-inactive in the cubic phase), at a few representative pressures. Navy dots exhibit measured data. The Lorentzian fits shown as pale green and orange areas represent the  $E_g$  and  $B_{2g}$  modes, respectively, and the red curves show the sum of the two modelled Lorentzian contributions.

One of the key observations in the high-pressure spectra is the presence of two peaks  $\approx 390\text{ cm}^{-1}$  above 19.2 GPa (Figures 3 and 4a). This is a single peak in the pressure range between 8.4 and 18.6 GPa, whose extrapolation down to 0 GPa arrives at a frequency around  $370\text{ cm}^{-1}$ . This frequency corresponds to a Raman-inactive, zone-boundary  $R_5^+$  phonon, which describes the scissor mode of the octahedra in the  $Pm\bar{3}m$  phase, according to the DFT calculations [24,25]. According to the symmetry analysis, this mode is supposed to split into two Raman-active modes ( $E_g$  and  $B_{2g}$ ) in the tetragonal  $I4/mcm$  structure, three Raman-active modes ( $B_{2g}$ ,  $B_{3g}$ , and  $A_g$ ) in the orthorhombic  $Imma$  structure, and one Raman-active ( $E_g$ ) and another Raman-inactive ( $A_{2g}$ ) modes in the rhombohedral  $R\bar{3}c$  structure. Therefore, the appearance of a single peak above 8.4 GPa and its splitting above 19.2 GPa are again supportive of the two successive structural phase transitions at each pressure, i.e., one from the cubic to the rhombohedral structure and another from the rhombohedral to the tetragonal structure.

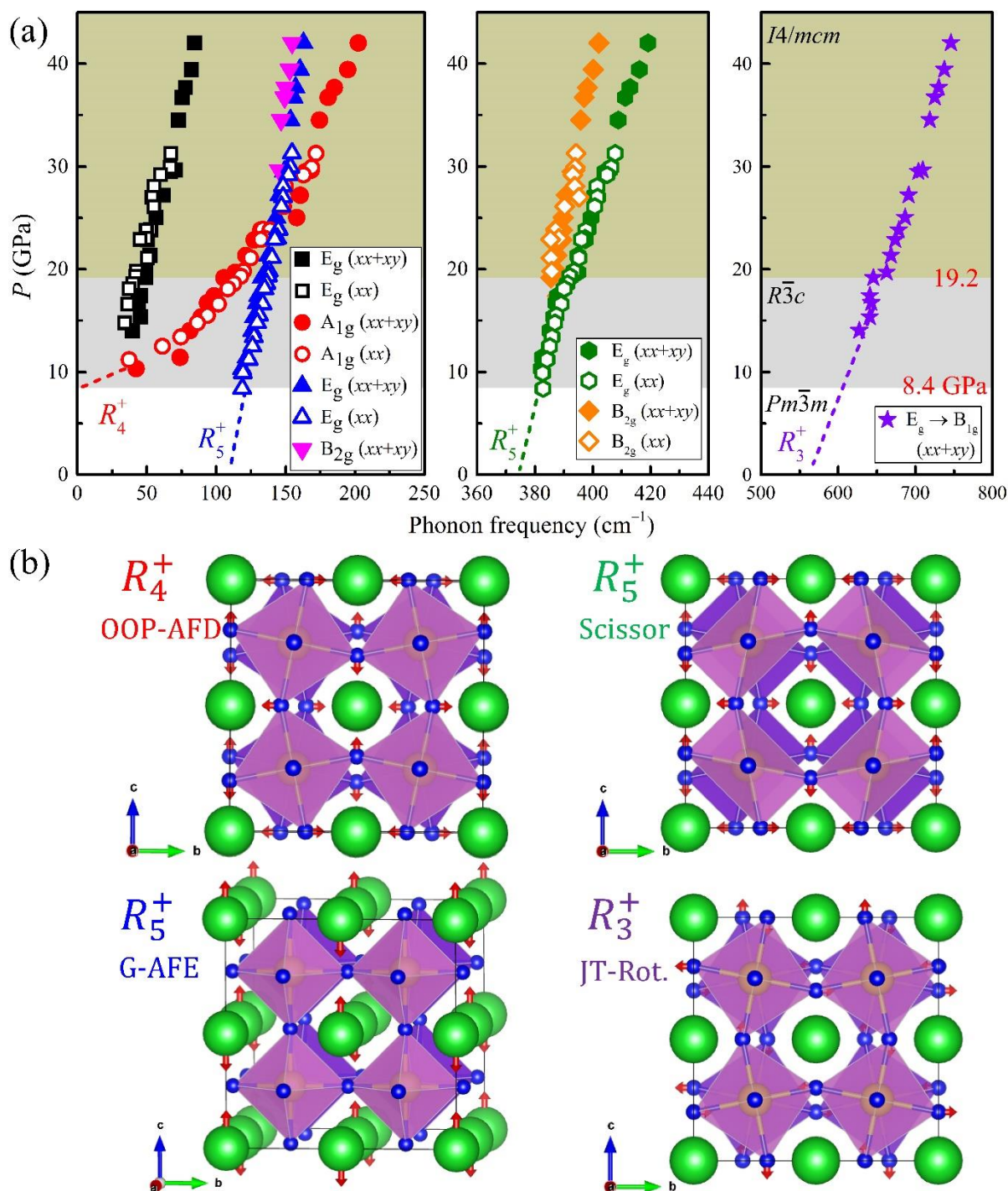


**Figure 4.** (a) Evolution of the Raman mode frequencies with variation in pressure. Open and solid marks are obtained from Figure 3a,b, respectively. Dashed lines represent the putative extension of each mode to zero pressure. (b) Atomic displacements of  $R$  point phonons illustrated on the  $2 \times 2 \times 2$  supercell with red arrows. Note that the lattice deformations are exaggerated. Here, the acronyms refer to out-of-phase antiferrodistortive mode (OOP-AFD), G-type antiferroelectric mode (G-AFE), scissor mode (Scissor), and Jahn–Teller-like rotation mode (JT-Rot).

Among the two separated modes, the strength of the  $B_{2g}$  peak should be suppressed in the parallel-polarized spectra by symmetry. Despite the finite leakage from the diamond anvils, the relative amplitude of the peaks with lower energies (marked with orange lozenges) is clearly reduced in the parallel-polarized spectra (Figure 3a). Therefore, we



could further assign the different symmetries of the two peaks; one with lower frequency can be assigned to the  $B_{2g}$  and the other to the  $E_g$  mode. The splitting of the peak into two above 19.2 GPa agrees well with the data of polycrystals [19]. Nonetheless, the authors in [19] interpreted the peak splitting as a signature of a phase transition from the  $R\bar{3}c$  to the  $Imma$ , which requires three split peaks above 19.2 GPa. We believe this assignment is inconsistent with the experimental finding of the two peaks above 19.2 GPa.

The emergence of other peaks is also consistent with multiple phase transitions. The high-frequency peak located  $\sim 630\text{ cm}^{-1}$  starts to appear above  $\sim 14$  GPa and increases its frequency with increasing pressure. Therefore, its Raman frequency is extrapolated to  $\sim 580\text{ cm}^{-1}$  upon being extended into 0 GPa, as indicated by a violet dashed line in Figure 4a. The mode frequency of  $\sim 560\text{ cm}^{-1}$  at 0 GPa is roughly close to the  $R_3^+$  mode frequency of  $545\text{ cm}^{-1}$  (Table 1) in the cubic symmetry, which describes the Jahn–Teller-like rotation mode of the octahedra according to the DFT calculations [24,25]. The Jahn–Teller-like rotation mode generates one Raman-active  $E_g$  mode in the  $R\bar{3}c$  phase and one Raman-active  $B_{1g}$  mode in the tetragonal phase, consistent with the observed data. The peak abruptly gains intensity above 19.2 GPa in the unpolarized spectra (Figure 3b) while it remains silent in the parallel-polarized spectra (Figure 3a). As the  $B_{1g}$  mode is generally known to appear in the cross-polarization spectra, the strongly enhanced intensity above 19.2 GPa clearly supports the assignment of the phonon mode to the  $B_{1g}$  symmetry in the tetragonal phase. If the system were to exhibit the orthorhombic  $Imma$  symmetry, this mode would result in two Raman-active modes. Therefore, the evolution of the  $E_g$  mode in the  $R\bar{3}c$  phase into only one  $B_{1g}$  mode above 19.2 GPa again supports that the structural phase transition at 19.2 GPa should be from the rhombohedral to the tetragonal structure.

Another peak located at  $120\text{ cm}^{-1}$  develops in the  $R\bar{3}c$  phase above 8.4 GPa and extrapolates to a frequency of  $\sim 110\text{ cm}^{-1}$  at 0 GPa, which is close to the  $R_5^+$  mode frequency of  $106\text{ cm}^{-1}$  (Table 1) as predicted by the DFT calculations for describing the antiphase antiferroelectric (AFE) motions of Ba atoms [24,25]. The observation of one mode is consistent with the prediction that there exists one Raman-active mode ( $E_g$ ) and one Raman-inactive mode ( $A_{2g}$ ) in the  $R\bar{3}c$  phase. At pressures above 19.2 GPa in the tetragonal  $I4/mcm$  structure, it is expected to present two Raman-active modes ( $E_g$  and  $B_{2g}$ ). Remarkably, we were able to resolve the two peaks above 30 GPa due to the considerable overlap of the two modes (inverted magenta and upright blue triangles in Figures 3a,b and 4). Furthermore, the higher-frequency peak (upright blue triangles) survives in the parallel-polarized spectra (Figure 3a), which is expected for the  $E_g$  mode. Accordingly, the peak with a lower frequency (inverted magenta triangles) is assigned as the  $B_{2g}$  mode.

At the lowest measured frequencies, two peaks located  $\sim 43\text{ cm}^{-1}$  appear above 10.3 GPa, which can be assigned as the out-of-phase AFD  $R_4^+$  soft mode [24,25]. In the cubic symmetry at 0 GPa, this AFD mode ( $R_4^+$ ) should be close to  $\sim 48\text{ cm}^{-1}$  according to the DFT calculations (Table 1). However, due to the soft mode feature, the  $R_4^+$  mode frequency near the structural phase boundary of 8.4 GPa is extrapolated to become zero. At higher pressures above 8.4 GPa, this AFD mode seems to gradually split into doubly degenerate  $E_g$  and nondegenerate  $A_{1g}$  modes, both of which are stabilized in both  $R\bar{3}c$  and  $I4/mcm$  phases. The two corresponding modes can be clearly distinguished above 11.4 GPa, and their frequencies become further apart with increasing pressure. The relative intensity of the higher-frequency mode (red circles) is pronounced in the parallel-polarized spectra corresponding to the  $A_{1g}$  irrep, while the lower-frequency  $E_g$  peak (black squares) exhibits a robust relative intensity in both the polarized and unpolarized spectra as compared to the other  $E_g$  modes.

In the assignment of the crystal symmetry based on the Raman spectra, there is always a possibility that the actual crystal symmetry may be lower than the assignment—as the expected Raman-active modes in a given structure may not be fully resolved in the experiments. Therefore, to validate the assigned crystal symmetry in the high-pressure range, it is worthwhile to compare at least the number of measured phonons with the expected ones based on the symmetries. It is known in the rhombohedral  $R\bar{3}c$  perovskites

that among the total 18 optical phonons ( $A_{1g} + 2A_{1u} + 3A_{2g} + 3A_{2u} + 5E_u + 4E_g$ ), only 5 optical phonons ( $A_{1g} + 4E_g$ ) can appear in the Raman spectra. Besides this, in the tetragonal  $I4/mcm$  perovskites, among the total 19 optical phonons ( $A_{1g} + A_{1u} + 2A_{2g} + 3A_{2u} + B_{1g} + B_{1u} + 2B_{2g} + 5E_u + 3E_g$ ), only 7 optical phonons ( $A_{1g} + B_{1g} + 2B_{2g} + 3E_g$ ) are known to become Raman-active. As summarized in Figure 4a, all the expected number of phonons for the assigned crystal symmetry were indeed confirmed, namely the five modes above 8.4 GPa and the seven modes above 19.2 GPa. Consequently, the observed high-pressure Raman modes coherently support a two-step structural transition from the cubic to rhombohedral to tetragonal phases, and all the irreps of the modes can be successfully assigned according to each lattice structure.

It should be noted that the pressure-dependent measurements presented in Figure 3a,b, albeit from independent two runs, have exhibited nearly-consistent phonon mode behaviors, as confirmed in the open and solid symbols in Figure 4a. On the other hand, given that the 4:1 methanol–ethanol liquid used as the pressure medium freezes and starts to lose hydrostaticity from 10 GPa, it might still be necessary to confirm the experimental observations by using a different pressure medium offering more reliable hydrostatic conditions. Hence, the pressure-dependent Raman experiment was repeated using NaCl as a pressure medium, which is known to provide decent quasi-hydrostaticity up to a pressure above 20 GPa [41], comparable to inert gases such as  $N_2$  and Ar [42]. As summarized in Figure S1 of the Supplementary Materials, the first structural transition is found at 8.9 GPa, and the second transition occurs at a pressure above 18.6 GPa when NaCl is used. In addition, the observed phonon evolutions in the two pressure ranges ( $8.9 \leq P \leq 18.6$  GPa, and  $18.6 \text{ GPa} < P$ ) are consistent with the results measured with the 4:1 methanol–ethanol mixture in Figures 3 and 4. Based on these results, we conclude that the two pressure-induced phase transitions should be understood as the inherent nature of BZO crystals independent of the choice of pressure medium.

It is worthwhile discussing how structural transitions may occur in BZO upon the application of pressure. Firstly, the large ionic radius of Ba as well as the smaller ionic charge of  $Ba^{2+}$  relative to  $Zr^{4+}$  ensures that the compressibility of the  $BaO_{12}$  polyhedra becomes greater than that of the  $ZrO_6$  octahedra, causing the  $ZrO_6$  octahedra to tilt under pressure [43]. Secondly, if the octahedra rotations bring the oxygen atoms and their next-nearest-neighbor Zr atoms closer, the hybridization between the empty Zr-3d and O-2p states renders the next-nearest-neighbor Zr–O interactions stronger to drive the AFD distortion [43]. Finally, continuous lattice deformation by applied pressures should yield an elastic strain that renormalizes the structural anisotropy from  $[111]_{pc}$  to  $[001]_{pc}$  [26]. Therefore, the energetic stability of the  $R\bar{3}c$  and  $I4/mcm$  phases can be switched by compression, in agreement with the observed second transition at 19.2 GPa.

A recent Brillouin scattering experiment [21] claimed that the inversion symmetry breaking may occur in BZO at room temperature and ambient pressure in a form of short-ranged ferroelectric (FE) distortions. If the claim is true, one may argue that the intermediate  $R\bar{3}c$  state may be helpful to develop a short-range FE distortion near the Ba site by stabilizing the noncentrosymmetric  $R3c$  phase at ambient pressure. However, the FE mode which takes the  $R\bar{3}c$  structure to the noncentrosymmetric  $R3c$  phase should involve considerable Ba displacements, which is unlikely to occur for the large  $Ba^{2+}$  ions [44]. Furthermore, if the short-range FE distortion occurs at the Zr sites, it is expected that the phonon modes found in the IR spectra should also become Raman-active. However, no sign of the first-order Raman-active phonon mode was found at ambient pressure, supporting that inversion symmetry was preserved in the high-quality BZO single crystal synthesized by optical floating-zone technique.

#### 4. Conclusions

In conclusion, the structure of  $BaZrO_3$  single crystals has been determined at atmospheric and high pressures by Raman scattering measurement. All the Raman modes observed at ambient pressure can be assigned to the multi-phonon scatterings allowed in

the cubic perovskite structure by referring to the complementary infrared phonon data and recent DFT calculations. Based on the observation of the appearance of new peaks at high pressures and their splitting, two pressure-induced structural phase transitions were identified:  $Pm\bar{3}m \rightarrow R\bar{3}c$  at 8.4 GPa and  $R\bar{3}c \rightarrow I4/mcm$  at 19.2 GPa. The evolution of the spectra at high pressures undoubtedly originates from the octahedra rotations; therefore, the absence of such features at atmospheric pressure corroborates the cubic  $Pm\bar{3}m$  structure as the ground state of  $BaZrO_3$  near 0 GPa. Moreover, the results imply that the  $R\bar{3}c$  structure is closer to the ground state than the  $I4/mcm$  or  $Imma$  phases. It is expected that the comprehensive understanding of the intrinsic structural phases of the BZO crystal could be helpful for strain engineering or chemical substitution, as well as the characterizations of other crystalline forms such as ceramics and nanocrystals relevant to industrial applications.

**Supplementary Materials:** The following supporting information can be downloaded at: <https://www.mdpi.com/article/10.3390/ma15124286/s1>, Figure S1: High-pressure evolution of  $BaZrO_3$  phonons measured with NaCl pressure medium.

**Author Contributions:** Conceptualization, D.-H.G. and K.H.K.; methodology, Y.S., Y.H.L., J.H.L., S.M. and Y.S.O.; validation, D.-H.G., S.M. and Y.S.O.; formal analysis, D.-H.G., S.M. and Y.S.O.; investigation, D.-H.G., S.M. and Y.S.O.; resources, Y.S.O.; data curation, D.-H.G., S.M. and Y.S.O.; writing—original draft preparation, D.-H.G.; writing—review and editing, S.M., Y.S.O. and K.H.K.; visualization, D.-H.G. and Y.S.O.; supervision, K.H.K.; project administration, K.H.K.; funding acquisition, S.M., Y.S.O. and K.H.K. All authors have read and agreed to the published version of the manuscript.

**Funding:** This research was financially supported by the National Research Foundation of Korea (NRF) grant funded by the Korean government (NRF-2019R1A2C2090648), the Korea Basic Science Institute (National Research Facilities and Equipment Center) grant funded by the Ministry of Education (grant no. 2021R1A6C101B418), and the Industry–University collaboration grant (0409-20200269) by Samsung Electronics. The work at HYU was supported by the National Research Foundation grant funded by the Korean government (MSIT) (2022R1F1A1072865). Y.S.O. acknowledges support from the Basic Science Research Programs through the National Research Foundation of Korea (2020R1A2C1009537).

**Institutional Review Board Statement:** Not applicable.

**Informed Consent Statement:** Not applicable.

**Conflicts of Interest:** The authors declare no conflict of interest.

## References

1. Vassen, R.; Cao, X.; Tietz, F.; Basu, D.; Stöver, D. Zirconates as New Materials for Thermal Barrier Coatings. *J. Am. Ceram. Soc.* **2000**, *83*, 2023. [[CrossRef](#)]
2. Liang, R.; Bonn, D.; Hardy, W.N. Growth of high quality YBCO single crystals using  $BaZrO_3$  crucibles. *Phys. C Supercond.* **1998**, *304*, 105. [[CrossRef](#)]
3. Azad, A.-M.; Subramaniam, S.; Dung, T.W. On the development of high density barium metazirconate ( $BaZrO_3$ ) ceramics. *J. Alloys Compd.* **2002**, *334*, 118. [[CrossRef](#)]
4. Roberts, S. Polarizabilities of Ions in Perovskite-Type Crystals. *Phys. Rev.* **1951**, *81*, 865. [[CrossRef](#)]
5. Muhsen, K.N.D.K.; Osman, R.A.M.; Idris, M.S. The effects of Ca, Zr and Sn substitutions into a ternary system of  $BaTiO_3$ – $BaSnO_3$ – $BaZrO_3$  towards its dielectric and piezoelectric properties: A review. *J. Mater. Sci. Mater. Electron.* **2020**, *32*, 12771. [[CrossRef](#)]
6. Parida, S.; Rout, S.; Cavalcante, L.; Sinha, E.; Li, M.S.; Subramanian, V.; Gupta, N.; Gupta, V.; Varela, J.A.; Longo, E. Structural refinement, optical and microwave dielectric properties of  $BaZrO_3$ . *Ceram. Int.* **2012**, *38*, 2129. [[CrossRef](#)]
7. Pergolesi, D.; Fabbri, E.; D’Epifanio, A.; Di Bartolomeo, E.; Tebano, A.; Sanna, S.; Licocchia, S.; Balestrino, G.; Traversa, E. High proton conduction in grain-boundary-free yttrium-doped barium zirconate films grown by pulsed laser deposition. *Nat. Mater.* **2010**, *9*, 846. [[CrossRef](#)]
8. Morejudo, S.H.; Zanón, R.; Escolástico, S.; Yuste-Tirados, I.; Malerød-Fjeld, H.; Vestre, P.K.; Coors, W.G.; Martínez, A.; Norby, T.; Serra, J.M.; et al. Direct conversion of methane to aromatics in a catalytic co-ionic membrane reactor. *Science* **2016**, *353*, 563. [[CrossRef](#)]

9. Malerød-Fjeld, H.; Clark, D.; Yuste-Tirados, I.; Zanón, R.; Catalán-Martinez, D.; Beeaff, D.; Morejudo, S.H.; Vestre, P.K.; Norby, T.; Haugsrud, R.; et al. Thermo-electrochemical production of compressed hydrogen from methane with near-zero energy loss. *Nat. Energy* **2017**, *2*, 923. [[CrossRef](#)]
10. Chen, X.; Rieth, L.; Miller, M.S.; Solzbacher, F. High temperature humidity sensors based on sputtered Y-doped BaZrO<sub>3</sub> thin films. *Sens. Actuators B Chem.* **2009**, *137*, 578. [[CrossRef](#)]
11. Akbarzadeh, A.; Kornev, I.; Malibert, C.; Bellaiche, L.; Kiat, J.-M. Combined theoretical and experimental study of the low-temperature properties of BaZrO<sub>3</sub>. *Phys. Rev. B* **2005**, *72*, 205104. [[CrossRef](#)]
12. Zhao, Y.; Weidner, D. Thermal expansion of SrZrO<sub>3</sub> and BaZrO<sub>3</sub> perovskites. *Phys. Chem. Miner.* **1991**, *18*, 294. [[CrossRef](#)]
13. Bilić, A.; Gale, J.D. Ground state structure of BaZrO<sub>3</sub>: A comparative first-principles study. *Phys. Rev. B* **2009**, *79*, 174107. [[CrossRef](#)]
14. Kersch, A.; Fischer, D.J. Phase stability and dielectric constant of ABO<sub>3</sub> perovskites from first principles. *Appl. Phys.* **2009**, *106*, 014105. [[CrossRef](#)]
15. Bennett, J.W.; Grinberg, I.; Rappe, A.M. Effect of symmetry lowering on the dielectric response of BaZrO<sub>3</sub>. *Phys. Rev. B* **2006**, *73*, 180102. [[CrossRef](#)]
16. Toulouse, C.; Amoroso, D.; Xin, C.; Veber, P.; Hatnean, M.C.; Balakrishnan, G.; Maglione, M.; Ghosez, P.; Kreisel, J.; Guennou, M. Lattice dynamics and Raman spectrum of BaZrO<sub>3</sub> single crystals. *Phys. Rev. B* **2019**, *100*, 134102. [[CrossRef](#)]
17. Lucazeau, G.J. Effect of pressure and temperature on Raman spectra of solids: Anharmonicity. *Raman Spectrosc.* **2003**, *34*, 478. [[CrossRef](#)]
18. Colomban, P.; Slodczyk, A. Raman Intensity: An Important Tool in the Study of Nanomaterials and Nanostructures. *Acta Phys. Pol. A* **2009**, *116*, 7. [[CrossRef](#)]
19. Chemarin, C.; Rosman, N.; Pagnier, T.; Lucazeau, G.J. A High-Pressure Raman Study of Mixed Perovskites BaCe<sub>x</sub>Zr<sub>1-x</sub>O<sub>3</sub> (0 ≤ x ≤ 1). *Solid State Chem.* **2000**, *149*, 298. [[CrossRef](#)]
20. Loudon, R. Theory of the first-order Raman effect in crystals. *Proc. R. Soc. A* **1963**, *275*, 218.
21. Helal, M.; Kojima, S. Structural instability and phase transition in BaZrO<sub>3</sub> single crystals: Brillouin scattering and DFT study. *Mater. Sci. Eng. B* **2021**, *271*, 115314. [[CrossRef](#)]
22. Sekine, T.; Uchinokura, K.; Matsuura, E. Raman scattering from two-phonon resonance states in SrTiO<sub>3</sub>. *Solid State Commun.* **1976**, *18*, 569. [[CrossRef](#)]
23. Perry, C.; Fertel, J.H.; McNelly, T.J. Temperature Dependence of the Raman Spectrum of SrTiO<sub>3</sub> and KTaO<sub>3</sub>. *Chem. Phys.* **1967**, *47*, 1619. [[CrossRef](#)]
24. Perrichon, A.; Jedvik Granhed, E.; Romanelli, G.; Piovano, A.; Lindman, A.; Hyldgaard, P.; Wahnstrom, G.; Karlsson, M. Unraveling the Ground-State Structure of BaZrO<sub>3</sub> by Neutron Scattering Experiments and First-Principles Calculations. *Chem. Mater.* **2020**, *32*, 2824. [[CrossRef](#)]
25. Granhed, E.J.; Wahnström, G.; Hyldgaard, P. BaZrO<sub>3</sub> stability under pressure: The role of nonlocal exchange and correlation. *Phys. Rev. B* **2020**, *101*, 224105. [[CrossRef](#)]
26. Chen, P.; Grisolia, M.N.; Zhao, H.J.; González-Vázquez, O.E.; Bellaiche, L.; Bibes, M.; Liu, B.-G.; Íñiguez, J. Energetics of oxygen-octahedra rotations in perovskite oxides from first principles. *Phys. Rev. B* **2018**, *97*, 024113. [[CrossRef](#)]
27. Lebedev, A.; Sluchinskaya, I. Combined first-principles and EXAFS study of structural instability in BaZrO<sub>3</sub>. *J. Adv. Dielectr.* **2015**, *5*, 1550019. [[CrossRef](#)]
28. Yang, X.; Li, Q.; Liu, R.; Liu, B.; Zhang, H.; Jiang, S.; Liu, J.; Zou, B.; Cui, T.; Liu, B. Structural phase transition of BaZrO<sub>3</sub> under high pressure. *J. Appl. Phys.* **2014**, *115*, 124907. [[CrossRef](#)]
29. Petzelt, J.; Ostapchuk, T.; Gregora, I.; Rychetsky, I.; Hoffmann-Eifert, S.; Pronin, A.; Yuzyuk, Y.; Gorshunov, B.; Kamba, S.; Bovtun, V.; et al. Dielectric, infrared, and Raman response of undoped SrTiO<sub>3</sub> ceramics: Evidence of polar grain boundaries. *Phys. Rev. B* **2001**, *64*, 184111. [[CrossRef](#)]
30. Jang, H.; Kumar, A.; Denev, S.; Biegalski, M.D.; Maksymovych, P.; Bark, C.; Nelson, C.T.; Folkman, C.; Baek, S.H.; Balke, N.; et al. Ferroelectricity in Strain-Free SrTiO<sub>3</sub> Thin Films. *Phys. Rev. Lett.* **2010**, *104*, 197601. [[CrossRef](#)]
31. Xin, C.; Veber, P.; Guennou, M.; Toulouse, C.; Valle, N.; Hatnean, M.C.; Balakrishnan, G.; Haumont, R.; Saint Martin, R.; Velazquez, M.; et al. Single crystal growth of BaZrO<sub>3</sub> from the melt at 2700 °C using optical floating zone technique and growth prospects from BaB<sub>2</sub>O<sub>4</sub> flux at 1350 °C. *Cryst. Eng. Comm.* **2019**, *21*, 502. [[CrossRef](#)]
32. Shen, G.; Wang, Y.; Dewaele, A.; Wu, C.; Fratanduono, D.E.; Eggert, J.; Klotz, S.; Dziubek, K.F.; Loubeyre, P.; Fat'yanov, O.V.; et al. Toward an international practical pressure scale: A proposal for an IPPS ruby gauge (IPPS-Ruby2020). *High Press. Res.* **2020**, *40*, 299. [[CrossRef](#)]
33. Mazzei, L.; Rukser, D.; Biebl, F.; Grimm-Lebsanft, B.; Neuber, G.; Pergolesi, D.; Börjesson, L.; Rübhausen, M.A.; Andreasson, J.; Karlsson, M.J. Phonon spectra of pure and acceptor doped BaZrO<sub>3</sub> investigated with visible and UV Raman spectroscopy. *Phys. Condens. Matter* **2020**, *32*, 405403. [[CrossRef](#)] [[PubMed](#)]
34. Shi, F.; Dong, H.; Liu, Q.; Yang, J.; Ren, S.; Sun, H.; Xiong, J. Investigation and theoretical calculation of the lattice vibrational spectra of BaZrO<sub>3</sub> ceramic. *J. Mater. Sci. Mater. Electron.* **2017**, *28*, 3467. [[CrossRef](#)]
35. Nuzhnyy, D.; Petzelt, J.; Savinov, M.; Ostapchuk, T.; Bovtun, V.; Kempa, M.; Hlinka, J.; Buscaglia, V.; Buscaglia, M.; Nanni, P. Broadband dielectric response of Ba(Zr,Ti)O<sub>3</sub> ceramics: From incipient relaxor and diffuse up to classical ferroelectric behavior. *Phys. Rev. B* **2012**, *86*, 014106. [[CrossRef](#)]

36. Stokes, H.T.; Kisi, E.H.; Hatch, D.M.; Howard, C.J. Group-theoretical analysis of octahedral tilting in ferroelectric perovskites. *Acta Crystallogr. B Struct. Sci.* **2002**, *58*, 934. [[CrossRef](#)]
37. Howard, C.J.; Stokes, H.T. Group-Theoretical Analysis of Octahedral Tilting in Perovskites. *Acta Crystallogr. B Struct. Sci.* **1998**, *54*, 782. [[CrossRef](#)]
38. Loudon, R. General Space-Group Selection Rules for Two-Phonon Processes. *Phys. Rev.* **1965**, *137*, A1784. [[CrossRef](#)]
39. Burns, G.; Dacol, F. Lattice modes in ferroelectric perovskites. III. Soft modes in BaTiO<sub>3</sub>. *Phys. Rev. B* **1978**, *18*, 5750. [[CrossRef](#)]
40. Husson, E.; Abello, L.; Morell, A. Short-range order in PbMg<sub>1/3</sub>Nb<sub>2/3</sub>O<sub>3</sub> ceramics by Raman spectroscopy. *Mater. Res. Bull.* **1990**, *25*, 539. [[CrossRef](#)]
41. Celeste, A.; Borondics, F.; Capitani, F. Hydrostaticity of pressure-transmitting media for high pressure infrared spectroscopy. *High Press. Res.* **2019**, *39*, 608. [[CrossRef](#)]
42. Klotz, S.; Chervin, J.-C.; Munsch, P.; Le Marchand, G.J. Hydrostatic limits of 11 pressure transmitting media. *Phys. D Appl. Phys.* **2009**, *42*, 075413. [[CrossRef](#)]
43. Xiang, H.; Guennou, M.; Íñiguez, J.; Kreisel, J.; Bellaiche, L. Rules and mechanisms governing octahedral tilts in perovskites under pressure. *Phys. Rev. B* **2017**, *96*, 054102. [[CrossRef](#)]
44. Benedek, N.A.; Fennie, C.J. Why Are There So Few Perovskite Ferroelectrics? *J. Phys. Chem. C* **2013**, *117*, 13339. [[CrossRef](#)]